Spontaneous Self-Assembly of Silver Nanoparticles into Lamellar Structured Silver Nanoleaves

Lun Li and Qiangbin Wang*

Suzhou Key Laboratory of Nanobiomedical Characterization, Division of Nanobiomedicine and *i*-Lab, Suzhou Institute of Nano-Tech and Nano-Bionics, Chinese Academy of Sciences, Suzhou 215123, P. R. China

ABSTRACT Uniform lamellar silver nanoleaves (AgNLs) were spontaneously assembled from 4 nm silver nanoparticles (AgNPs) with *p*-aminothiophenol (PATP) as mediator under mild shaking at room temperature. The compositions of the AgNLs were verified to be ~1 nm Ag_{25} nanoclusters and PATP molecules in quinonoid model. The underlying assembly mechanism was systematically investigated and a two-step reaction process was proposed. First, the 4 nm AgNPs were quickly etched to ~1 nm Ag_{25} nanoclusters by PATP in the form of $[Ag_{25}(PATP)_n]^{n+}$ ($n < 12$), which were then further electrostatically or covalently interconnected by PATP to form the repeated unit cells of $[Ag_{25}(PATP)_{n-1}]^{(n-1)+}$—PATP—$[Ag_{25}(PATP)_{n-1}]^{(n-1)+}$ (abbreviated as Ag_{25}—PATP—Ag_{25}). Second, these Ag_{25}—PATP—Ag_{25} complexes were employed as building blocks to construct lamellar AgNLs under the directions of the strong dipole—dipole interaction and the $\pi-\pi$ stacking force between the neighboring benzene rings of PATP. Different reaction parameters including the types and concentrations of ligands, solvents, reaction temperature, ionic strength, and pH, *etc.*, were carefully studied to confirm this mechanism. Finally, the preliminary investigations of the applications for AgNLs as "molecular junctions" and SERS properties were demonstrated. We expect that this convenient and simple method can be in principle extended to other systems, or even mixture system with different types of NPs, and will provide an important avenue for designing metamaterials and exploring their physicochemical properties.

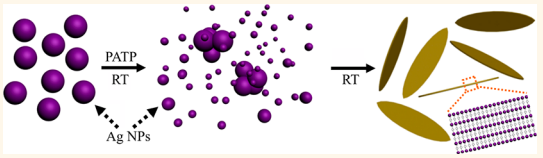

KEYWORDS: silver nanoparticles · silver nanoleaves · self-assembly · metamaterials · lamellar nanostructures

The last decades have witnessed tremendous progress in the preparation of different kinds of nanocrystals (NCs) with controlled sizes, morphologies, compositions, and surface functionalities. These NCs exhibit appealing electronic, magnetic, and photonic properties and have attracted great efforts to be manipulated as "artificial atoms".[1−11] As an important "bottom-up" method, the self-assembly of these NCs into desirable metamaterials in a highly efficient manners could provide an opportunity to investigate and further tailor their collective physical properties.[12,13] Until recently, although many strategies to obtain metamaterials, such as solution crystallization, wet deposition, interfacial organization, and the biomolecular-directed self-assembly, have already been developed,[14−20] some disadvantages of these methods such as them being time-consuming, labor-consuming, or costly hinder their wide applications. Assembling the NCs into uniform entities by a convenient and simple way still remains a critical challenge.

Herein, a facile method was discovered to controllably assemble the Ag nanoparticles (AgNPs) into lamellar structured Ag nanoleaves (AgNLs) by simply mixing cyclohexane containing 4 nm AgNPs and ethanol containing *p*-aminothiophenol (PATP) at room temperature (RT). In a typical process, 50 μL of cyclohexane containing AgNPs (~10 mM of [Ag]) was mixed with 400 μL of ethanol containing PATP (50 mM) at RT. Then the mixture was subjected to a mild shaking at 800 rpm for 4 h and uniform lamellar AgNLs were obtained after purification. Although some previous reported methods have produced analogous noble metal lamellar nanostructures or even Au leaves using thiol ligands,[21−25] they lacked control over the uniform morphology and highly ordered structures. Herein, this solution process of preparing uniform, lamellar structured AgNLs was convenient and simple, as well as highly reproducible. Additionally, a preliminary conductivity investigation of the AgNLs was performed, and the result showed potential electron

* Address correspondence to qbwang2008@sinano.ac.cn.

Received for review September 26, 2012 and accepted March 22, 2013.

Published online March 23, 2013
10.1021/nn304450b

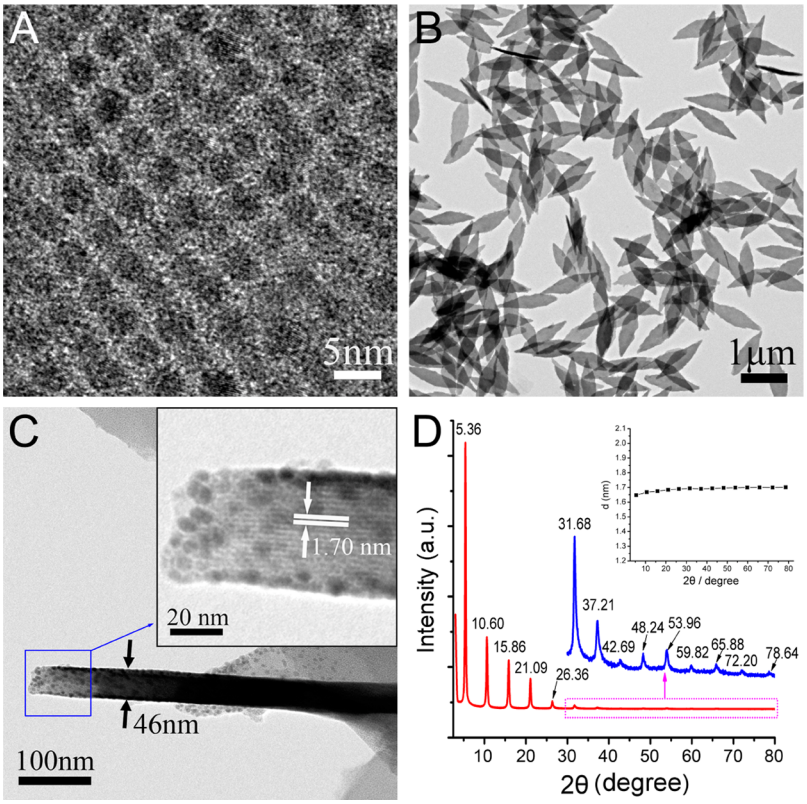

Figure 1. Characterizations of the AgNPs and AgNLs. (A) TEM image of the initial 4 nm-sized AgNPs; (B) the as-obtained AgNLs; (C) HRTEM image of a typical AgNL from side view. The inset was an enlarged view of the selected blue box; (D) WAXRD pattern of the AgNLs. The inset showed the calculated interlayer distance of the AgNLs with different diffraction peaks. The blue line presented the magnified view of the corresponding 2θ area. Corresponding values of 2θ for each diffraction peak were also given.

transfer properties with a gigohm level resistance, a benefit from the ordered arrangement of quinonoid model PATP molecules in the AgNLs which presented a large conjugated network throughout the AgNLs. Surface enhanced Raman spectroscopy (SERS) study showed that the AgNLs acted as an active SERS substrate with a significant enhancement factor on the order of 10^{12}∼10^{13} magnitude. These results will shed light on the future design and preparation of metamaterials, as well as the potential applications of AgNLs on optoelectronic devices.

RESULTS AND DISCUSSION

The typical transmission electron microscope (TEM) images of the initial 4 nm AgNPs which were prepared by using our previous method[26] were shown in Figure 1A,B. The formed AgNPs superlattices in Figure 1A illustrated their highly monodisperse nature with a standard deviation of 2.5% (see Supporting Information, Figures S1−S4 for more characterizations of the AgNPs). The TEM image of highly uniform AgNLs with a radial length of ∼1.25 μm and aspect ratio of ∼3.5 was presented as Figure 1B. The typical thickness of the AgNL from side view determined by TEM showed its value of ∼46 nm (Figure 1C), and the highly ordered lamellar feature of the AgNL was proved by the inset high-resolution TEM (HRTEM) image of a ∼1.7 nm interlayer distance. In Figure 1C, it can be seen that some bigger AgNPs with size > 5 nm were attached on the outer surface of the AgNLs (see later for more detailed discussion). The wide-angle X-ray diffraction (WAXRD) pattern in Figure 1D further verified the lamellar feature of the as-obtained AgNLs with the unprecedented 14th periodic diffraction peaks. The average interlayer distance (denoted as **d**) of the AgNLs from the WAXRD data was calculated to be 1.6881 nm using the Bragg's law (inset of Figure 1D, Supporting Information, Figure S5 and Table S1), which was well consistent with the value measured by HRTEM.

It was very interesting that AgNPs were controllably assembled into lamellar AgNLs in such a facile way without an extra procedure needed. To fully understand the underlying formation mechanism of AgNLs, two key issues were raised to be solved: (i) What was the building block of the AgNLs with skeleton length of ∼1.7 nm? (ii) What were the dominant driving forces to direct the self-assembly process?

To answer the first question, electron microscope (EM) measurements were first performed to analyze the components of the AgNLs. As the scanning TEM (STEM) image of the AgNL presented in Figure 2A, combined with the selected area electron diffraction

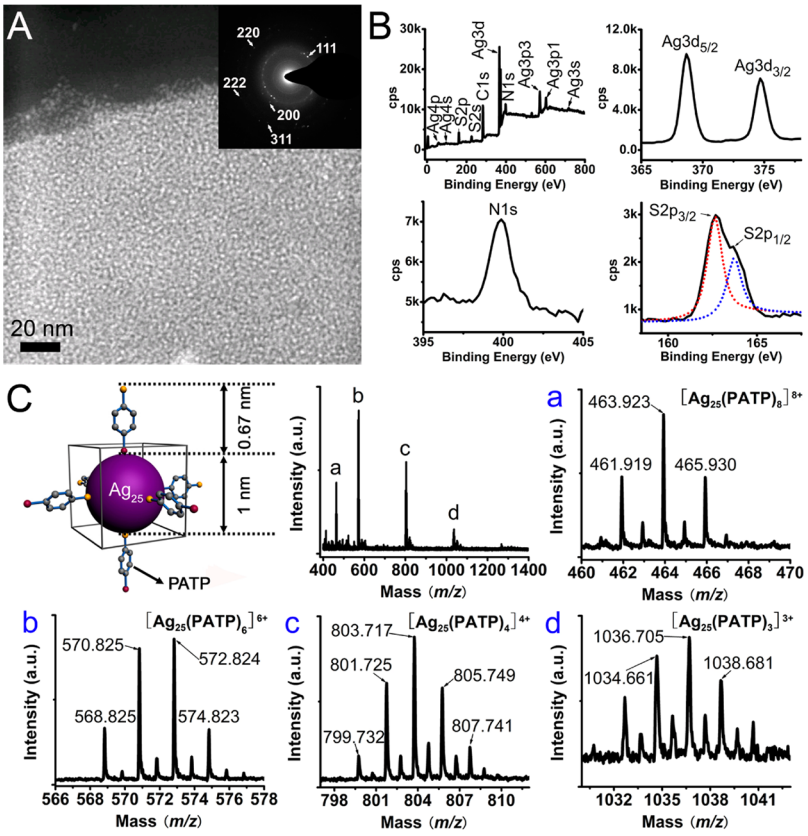

Figure 2. Component analysis of the AgNLs. (A) STEM image of a typical AgNL, wherein the white dots presented small Ag nanoclusters composed of the AgNLs. The inset SAED of this AgNL also clearly showed four diffraction rings of Ag element. (B) XPS results of the AgNLs. The molar ratio of N:S:Ag was determined to be 0.30:0.30:1. (C) MALDI-TOF-MS spectrum of the AgNLs. The upper-left corner presented the schematic illustration of Ag_{25} nanoclusters attached with six PATP in 3D space.

(SAED, inset in Figure 2A), STEM images (Supporting Information, Figure S6) and energy-dispersive spectroscopy (EDS, Figure S7), the AgNLs were found to be composed of small AgNPs with a size less than 2 nm. This suggested that the initial 4 nm AgNPs underwent a decomposition process to form the smaller Ag nanoclusters during the assembling process. It has been well documented that the thiol group containing molecules can effectively exchange the ligands on the surface of the Au or Ag NCs, and then etch them into smaller species.[27,28] As to our reaction system, we concluded that the thiol-containing ligands PATP could also act as etchants to decompose the initial AgNPs into smaller Ag nanoclusters. To verify this hypothesis, the UV−vis spectrum was performed to monitor the reaction at the early reaction stage (Supporting Information, Figure S8). It was found the intrinsic absorbance peak of Ag was blued-shifted from 412 to 400 nm in the first 2 min after mixing the AgNPs and the PATP solution, which indicated the formation of smaller Ag nanoclusters in the reaction. Meanwhile, the simultaneous aggregations or recrystallizations from the original AgNPs and the newly formed smaller Ag nanoclusters into bigger AgNPs were also observed under TEM (Supporting Information, Figure S9), showing the same phenomenon as aforementioned in Figure 1C.

X-ray photoelectron spectroscopy (XPS) was then allowed to probe the chemical states of Ag and PATP in AgNLs and then disclose the interaction between Ag and PATP.[29] Figure 2B presents the high-resolution XPS results of Ag3d, S2p, and N1s, wherein the binding energies of $Ag3d_{5/2}$ and $Ag3d_{3/2}$ were basically the same as the standard values of 368.72 and 374.64 eV, respectively, illustrating the zerovalent state of Ag. Meanwhile, the binding energies of $S2p_{3/2}$ (162.66 eV) and $S2p_{1/2}$ (163.70 eV) were 1.24 and 1.4 eV less than the standard values, respectively, and the binding energy of N1s (399.87 eV) was 1.47 eV higher than the standard value, indicative of negative and positive charge states of the S and N elements in PATP. Thus, the XPS results proved that the PATP was in quinonoid model in the AgNLs and the newly formed Ag nanoclusters were electrostatically/covalently bound with the −SH and $-NH_2$ in PATP to form $[Ag_m(PATP)_n]^{n+}$ complexes according to previous reports.[21,30] The electrostatic and/or covalent binding of the ligand with Ag nanoclusters was investigated in detail and was found to be dominant in the assembly of AgNPs into uniform lamellar AgNLs. Weakening the electrostatic and/or covalent binding energies resulted in less uniform lamellar products in different morphologies. For example, if PATP was replaced by a ligand with

either one or none of the functional groups of −SH and $-NH_2$, irregular products were obtained (Supporting Information, Figure S10).

The matrix-assisted laser desorption/ionization time-of-flight mass spectrometry (MALDI-TOF-MS) in the positive reflector mode was further performed to determine the accurate components of the AgNLs.[28,29] Four prominent peaks of *m/z* in Figure 2C were calculated to be in accordance with the structure form of $[Ag_{25}(PATP)_n]^{n+}$ ($n < 12$) and the highest signal was assigned to $[Ag_{25}(PATP)_6]^{6+}$ (Figure 2Cb; for more information see Supporting Information, Tables S2−S3 and Figure S11), which evidenced that the Ag_{25} nanoclusters were the sole format of Ag in AgNLs and the $[Ag_{25}(PATP)_6]^{6+}$ species were the main component of the AgNLs. Ideally, when six PATP molecules were attached to one Ag_{25} nanocluster, they would stand up vertically and prefer to occupy the center of one plane of the Ag_{25} nanocluster in 3D space, similar to the face-centered cubic structure, as presented in the upper-left corner of Figure 2C. Surprisingly, the size of the Ag_{25} nanoclusters was estimated to be ∼1 nm, which was unexpectedly consistent with the observed size in Figure 2A.

On the basis of the above results, the main component of AgNLs has been determined as $[Ag_{25}(PATP)_6]^{6+}$. Owing to strong electrostatical/covalent interaction between the thiol/amino group of PATP and Ag,[21] $[Ag_{25}(PATP)_6]^{6+}$ structures will be further interconnected to form the $[Ag_{25}(PATP)_5]^{5+}$-PATP-$[Ag_{25}(PATP)_5]^{5+}$ (abbreviated as Ag_{25}−PATP−Ag_{25}). With a 3D modeling using Chem3D Ultra software (Supporting Information, Figure S12), the skeleton length of the PATP in the quinonoid model was estimated at ∼0.67 nm, thus rendering the linear length of the Ag_{25}−PATP−Ag_{25} around 1.67 nm. This value was perfectly consistent with the observed interlayer distance determined by HRTEM and WAXRD. Therefore, we concluded that the Ag_{25}−PATP−Ag_{25} functioned as the building block to be assembled into the highly ordered lamellar AgNLs.

Regarding the driving force for the formation of the highly ordered lamellar AgNLs from the building block Ag_{25}−PATP−Ag_{25}, we attributed it to the strong dipole−dipole attraction[31,32] and $\pi-\pi$ stacking force[33,34] between the neighboring benzene rings in PATP, which directed the assembly of AgNPs into AgNLs. Tang and co-workers have successfully demonstrated the important role of dipole−dipole interaction in assembly of single CdTe NPs into 1D wires or 2D sheets.[31,32] Regarding our reaction system, XPS and MALDI-TOF-MS data have supported the quinonoid model of PATP with an electron-donor group ($-NH_2$) and an electron-acceptor group (−SH) connected by a conjugated π system, which further interacted electrostatically/covalently with newly formed Ag_{25} nanoclusters to form Ag_{25}−PATP−Ag_{25} as the building block of the lamellar AgNLs. As shown in Figure 2C, most of the Ag_{25} nanoclusters were coated with six copies of PATP, in which each PATP occupied one plane of the Ag_{25} nanocluster in a 3D space. When the Ag_{25} nanoclusters were assembled in solution, the dipole−dipole interaction guided their assembling head-to-head to form Ag_{25}−PATP−Ag_{25} complexes, which were also energy favorable due to the minimized steric repulsion and entropy.[35]

The contribution of the dipole−dipole interaction on the self-assembly of highly ordered lamellar AgNLs was confirmed by a series of control experiments, including the ionic strength, the pH, and the solvents, *etc.* (Supporting Information, Figure S13−S19). With weakened dipole−dipole interaction between the Ag_{25}−PATP−Ag_{25} complexes, much less ordered lamellar products were obtained. As shown in Supporting Information, Figure S13, most of the products in irregular morphologies were obtained with up to six periodic diffraction peaks in a 1 M $MgCl_2$ solution, due to the enhanced electrostatic screening effect of Mg^{2+} ions in the reaction solution which decreased the electrostatic interaction between PATP and Ag_{25} nanoclusters. As well, the pH and the polarity of the solvents in the reaction were also observed to influence the products with significantly different lamellar properties, in which the protonation and deprotonation of PATP under different pH and polarity conditions changed the electrostatic interaction and therefore resulted in the various ordered products (Supporting Information, Figures S14, S16, S17−S19).

Another important driving force for the ordered self-assembly of AgNLs was credited to the $\pi-\pi$ stacking of the aromatic rings in neighboring PATP in Ag_{25}−PATP−Ag_{25} skeletons. Under the guidance of the $\pi-\pi$ stacking force, the Ag_{25}−PATP−Ag_{25} complexes would prefer to assembly side-by-side parallelly on a horizontal plane. The contribution of the $\pi-\pi$ stacking force on the organization of lamellar AgNLs was verified in a list of control experiments. For example, because the $\pi-\pi$ stacking can be affected by the reaction temperature due to the interruption of the vibration resulted from the heating, the products obtained at 50 °C showed the decreased lamellar nature of the Ag flakes with no specific morphology (Supporting Information, Figure S20). This indicated that the decreased $\pi-\pi$ stacking brought about the less controllable assembly of AgNLs. In addition, by replacing the PAPT ligand with other ligands containing thiol and amine groups but without the aromatic ring, such as mercaptamine, no ordered lamellar product was obtained as shown in Supporting Information, Figure S21, compared with those obtained from ligands containing aromatic ring (Supporting Information, Figure S22). As a result, we proposed the formation mechanism of AgNL as illustrated in Figure 3, in which the 4 nm AgNPs were first etched into ∼1 nm Ag_{25} nanoclusters by PATP and then formed the

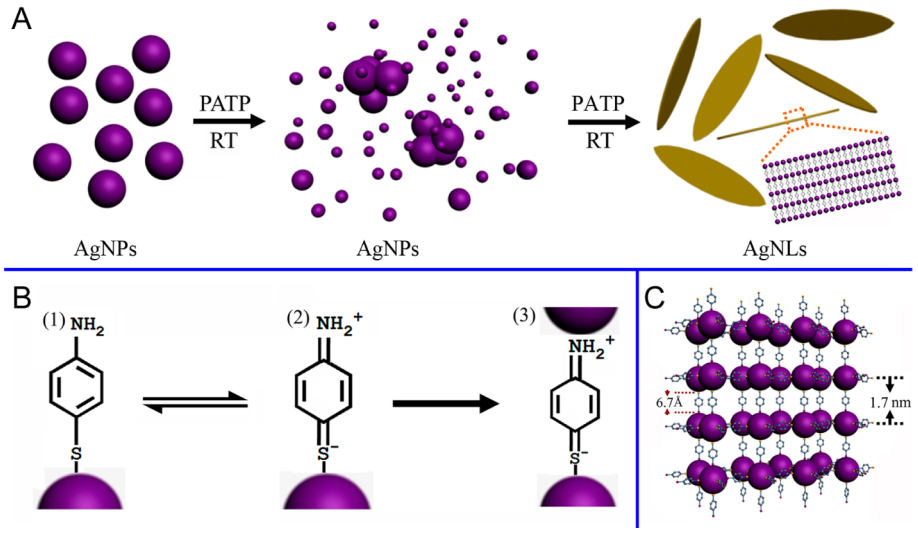

Figure 3. Formation mechanism of the AgNLs. (A) Schematic illustration for the process of forming lamellar AgNLs. (B) Two possible resonant states of PATP: (1) benzenoid and (2) quinonoid. The PATP in quinonoid model could electrostactically/covalently interconnect two Ag_{25} nanoclusters to form the Ag_{25}−PATP−Ag_{25} complex (3). (C) The 3D network of lamellar AgNLs with Ag_{25}−PATP−Ag_{25} of ∼1.7 nm skeleton length.

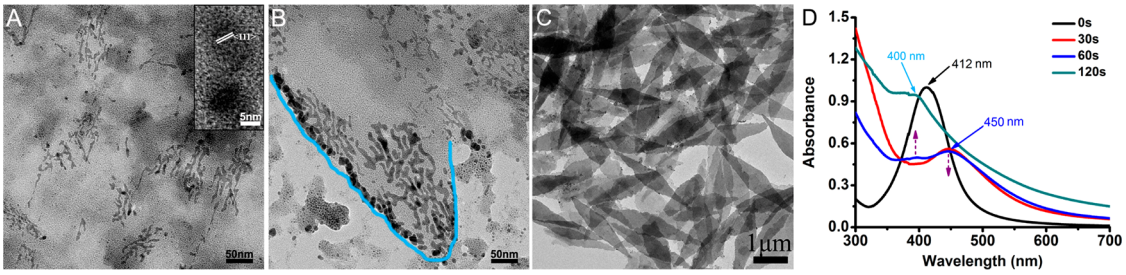

Figure 4. The growth evolution of the AgNLs in the early reaction stage. (A−C) TEM images of the products obtained from 30 s (A), 60 s (B), and 120 s (C) of the reaction system, respectively. Inset in Figure 4A showed the HRTEM images of the big aggregates of AgNPs. (D) The UV−vis spectrum obtained from the first reaction of 2 min.

Ag_{25}−PATP−Ag_{25} complex as the building block for the assembly of lamellar AgNLs under the guidance of the dipole−dipole interaction and the $\pi-\pi$ stacking of the benzene rings between the neighboring PATP molecules.

The evolution of the AgNLs was carefully studied using UV−vis spectrum and TEM to reveal how the AgNPs were assembled into AgNLs. Because the prototyped AgNLs could be successfully assembled in just 2 min (Figure 4C), no morphology changes of the AgNLs were observed in follow-up reactions even elongating to seven days (Supporting Information, Figures S23−S25). Therefore, it was very important to study the etching process and the follow-up assembling behavior during the first 2 min (Figure 4 and Supporting Information, Figures S26−28). Three samples were collected at 30, 60, and 120 s, respectively, to reveal the process. As shown in Figure 4A, we observed that there were some large AgNPs formed with sizes larger than 4 nm, besides the numerous etched AgNPs about 1 nm in size, in the first 30 s (Figure 4A and Supporting Information, Figure S27). When the reaction continued to 60 s, embryonic AgNLs were observed under the TEM images (Figure 4B and Supporting Information, Figure S28). When the reaction time was extended to 120 s, most of the newly formed ∼1 nm AgNPs assembled into AgNLs with the bigger AgNPs absorbed on the outer surface of the AgNLs (Figure 4C). We speculated that two processes happened in the 2 min reaction: (1) The 4 nm AgNPs were etched into ∼1 nm Ag_{25} nanoclusters after the mixing of AgNPs with PATP, followed by the formation of Ag_{25}−PATP−Ag_{25} complexes. Then the lamellar AgNLs assembled under the guidance of dipole−dipole interaction and the $\pi-\pi$ stacking force between the neighboring benzene rings in PATP molecules. (2) The recrystallization of the initial 4 nm AgNPs with the newly formed Ag_{25} nanoclusters resulted in the larger AgNPs observed in Figure 4A. Due to the incompatible size of the larger AgNPs with the dominant Ag_{25} nanoclusters, the larger sized AgNPs were gradually ejected from the body of the newly formed AgNLs onto the outer surface during the AgNL assembly. The UV−vis spectroscopy was also used to *in situ* monitor the reaction. As shown in Figure 4D, the initial 4 nm AgNPs presented a narrow absorbance peak at 412 nm.

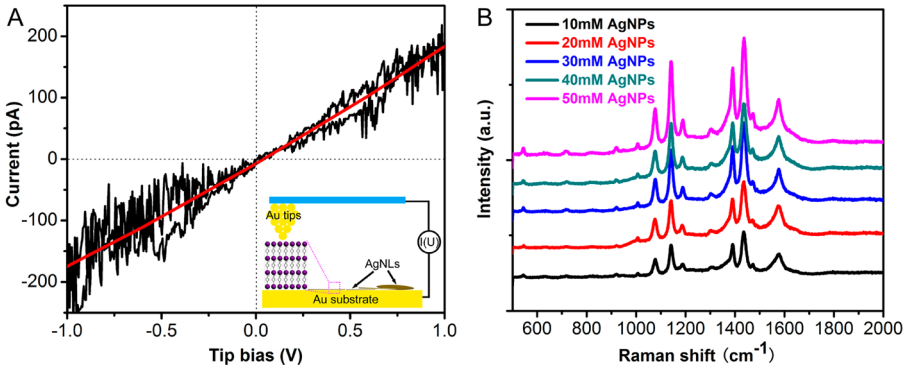

Figure 5. Two potential applications of the AgNLs. (A) A typical *I*−*V* curve of AgNLs measured by AFM. The experimental (black line) and simulated results (red line) between ±1 V were both presented. Inset in the lower right corner was the schematic illustration of the experimental setup, where the AgNLs were randomly attached to a sheet of gold substrate. (B) SERS spectra of the AgNLs. The AgNLs used in the two measurements were prepared as in Figure 1B. The SERS spectra obtained from five different sizes of AgNLs were also presented. Corresponding EM images of the AgNLs under 10, 20, 30, 40, 50 mM of AgNPs were shown in Supporting Information, Figure S35.

It is notable that, due to the quick reaction between the AgNPs and PATP, it was hard to capture the product at the point in time that the AgNLs and PATP were mixed (Supporting Information, Figure S26). However, after mixing the AgNPs and PATP for 30 s reaction, there were two peaks appearing at 400 and 450 nm, indicating that there were two populations of AgNPs formed. The absorbance peak at 400 nm presented the smaller AgNPs from the etching of 4 nm AgNPs, while the 450 nm absorbance peak identified the existence of larger AgNPs. Extending the reaction time to 60 s, we observed that a peak appeared in 400 nm and the 450 nm peak intensity decreased, suggesting that the ongoing etching process produced more and more Ag_{25} nanoclusters and the larger AgNP aggregates were gradually diminishing. With reaction time elongated to 120 s, a significant absorbance peak at 400 nm was observed and the absorbance peak at 450 nm completely vanished; this clearly illustrated that the ~1 nm Ag nanoclusters were dominant in the products and then were assembled into the AgNLs in the short time of 2 min as shown in Figure 4C.

Taking all together, we successfully developed a facile strategy to assemblea AgNP as an artificial atom into a highly ordered lamellar AgNL and then proposed its self-assembling mechanism. To generalize this method, we found that the lamellar AgNLs were obtained if the ligands met three prerequisites: (1) containing the thiol group to etch the big AgNPs into small ones; (2) containing a conjugated bond system to form Ag−linker−Ag nanostructure as building block; (3) containing a rigid benzene ring to guide the Ag−linker−Ag nanostructures assembling into ordered lamellar structures. In addition, the solvents should be able to provide good solubility of the ligands and the initial AgNPs for the assembling, respectively. All the results supported our conclusion that the strong dipole−dipole attraction and the $\pi-\pi$ stacking force originating from the linkers, as well as the solvent, played important roles in obtaining the desired lamellar Ag nanostructures.

Because the lamellar AgNLs were composed of highly ordered Ag_{25}−PATP−Ag_{25} complexes as building blocks, where the PATP presented a conjugated state of quinonoid model, one assumption was raised that these unique Ag_{25}−PATP−Ag_{25} complexes might work as "molecular junctions" and endow the lamellar AgNLs with conductive properties.[36,37] Therefore, the current−voltage (*I*−*V*) curve of the circuit by putting a single AgNL on Au substrate using AFM was performed. As shown in Figure 5A, a linear relationship between the current and voltage with a little hysteresis was observed. In the ohmic region from both the measured and simulated *I*−*V* curves, the AgNL possessed electric resistance on the order of gigohms (GΩ) by measuring over 50 AgNLs. This phenomenon suggested the charge transfer process indeed occurred throughout the profiles of the AgNLs with the junction gap up to 50 nm. We expected that this conductive property of AgNLs could further provide another platform for studying charge-transfer mechanisms between metal nanoclusters and even promote the future development of electronics devices. Additionally, the quantitative understanding of the relationship between the current and the size of AgNLs, different ligands, and so on are under investigation.

Moreover, we were also aware that the Ag substrate is an excellent candidate for SERS assay. Therefore, the SERS properties of the AgNLs were studied by using a 532-nm laser with applied power of 0.63 mW. As shown in Figure 5B, it was observed that, besides a major a_1 vibration band of PATP at 1079 cm^{-1}, there were three additional bands at 1142, 1391, and 1436 cm^{-1} appearing with considerable enhancement, which were assigned as the −N═N− stretching modes of 4,4′-dimercaptoazobenzene (DMAB) from the dimerization of PATP.[38−40] The estimated enhancement factors (EF) for the three bands were on the order of 10^{12}~10^{13}

magnitude (Supporting Information, Figure S29). We attributed this significant enhancement of DMAB on the surface of AgNLs to the highly ordered Ag_{25}−PATP−Ag_{25} sandwich nanostructures, wherein the dynamic charge transfer occurred between Ag_{25} nanoclusters through coupling with the vibrations of the bridging molecules of PATP.[41] It is worthy noting that the DMAB molecules were transformed from PATP on the outer surface of AgNLs by the Ag nanoclusters catalyzed photochemical reaction during SERS measurements, and the PATP located inside of the AgNLs were not dimerized into DMAB (see Supporting Information, Figures S30−34 for detailed discussion). Furthermore, we also found that under the same laser power, the SERS signals increased with an increase in the sizes of the AgNLs as shown in Figure 5B. The sizes of the AgNLs could be finely tuned by varying the molar ratios of the PATP/Ag (Supporting Information, Figures S35−S36). We mainly attributed this phenomenon to rougher surface and bigger AgNPs on the surface of AgNLs as envisioned in Supporting Information, Figure S35. With respect to the SERS assay, one additional point should be made that the AgNLs prepared by using this convenient and simple method were highly uniform in size and shape, which might help resolve the reproducibility problem of the SERS substrates.

CONCLUSION

We have reported a convenient and simple approach to spontaneously assemble AgNPs into uniformly lamellar AgNLs with PATP molecule as mediator. The self-assembly mechanism has been experimentally elucidated as (1) the formation of uniform ∼1 nm Ag_{25} nanoclusters obtained from the etching of 4 nm AgNPs by PATP; (2) the formation of the quinonoid model of PATP with the electrostatical/covalent interaction between −HS/−NH_2 and AgNP resulting in the Ag_{25}−PATP−Ag_{25} complex as a building block; (3) the strong dipole−dipole interaction and the $\pi-\pi$ stacking force between the neighboring rigid benzene skeleton of PATP induced the ordered organization of Ag_{25}−PATP−Ag_{25} complexes into lamellar AgNLs. We expect that this methodology will provide an important avenue for designing new metamaterials and exploring their novel physicochemical properties.

METHODS

Materials. All chemicals were used as received without further purification. $AgNO_3$ (99.8%), ethanol (99.7%), cyclohexane (99.5%) and other common solvents were purchased from Sinopharm Chemical Reagent Co, Ltd. Oleylamine (OAM, 70%), *p*-aminothiophenol (PATP, 97%) and other organics used in the control experiments were all obtained from Sigma Aldrich.

Assembly of Monodisperse AgNPs into AgNLs. The procedure to produce 4 nm AgNPs referred to our previous report.[26] The as-prepared AgNPs could be readily dispersed in cyclohexane. The typical procedure to produce the AgNLs as shown in Figure 1B had been presented in the last paragraph of the Introduction. Once the reaction was finished, the as-obtained AgNLs were washed with a large amount of ethanol for three times to remove excess PATP, and then they were resuspended into water. The AgNLs in different sizes (include radial length, aspect ratio, thickness) were produced by changing the concentration of [Ag] from 10, 20, 30, to 50 mM, respectively, while keeping the other parameters unchanged. The evolution of the AgNLs was studied by using 25 mM of [Ag] in the reaction while keeping other parameters unchanged.

Characterization. The morphologies of the as-synthesized products (AgNPs and AgNLs) were examined on a transmission electron microscope or scanning transmission electron microscope (TEM/STEM, Tecnai G2 F20 S-Twin) at an acceleration voltage of 200 KV, and a scanning electron microscopy (SEM, Quanta 400 FEG) at 10 KV, respectively. The radial length and thickness of the AgNLs were qualified by dropping the solution of the AgNLs onto mica to be measured on an AFM (Aligent 5500) after the samples were dried at 60 °C in the vacuum oven. Fourier transform infrared spectroscopy (FTIR) measurements of AgNPs and AgNLs were taken on aNicolet 6700 instrument. The SERS were recorded using JY HR 800 Confocal Raman spectrometer with a 100× objective lens (NA = 0.90). A 532-nm diode laser was applied as the excitation source, and a thermoelectrically cooled (−70 °C) CCD detector was used to collect the backscattered Raman signals with one acquisition of 10 s accumulation. UV−vis spectra were performed on a Lambda-25 spectrometer (Perkin-Elmer, USA) at RT. WAXRD patterns of the as-prepared products were recorded on a Bruker D8 Advance powder X-ray diffractometer at a scanning rate of 2° min^{-1}, using Cu Kα radiation (λ = 1.5406 Å) in the range of 20−80° for AgNPs and 1−80° for AgNLs, respectively. X-ray photoelectron spectroscopy (XPS) was performed on Perkin-Elmer PHI 5000C ESCA X-ray photoelectron spectrometer using Al Kα radiation (1486.6 eV) as the exciting source. The bonding energies of the AgNLs obtained from the XPS analysis were corrected for specimen charging by referencing the C1s to 284.80 eV. The 3D model structure of PATP molecules was optimized by chem3D Ultra 8.0 software. An XE-120 microscope (Park Systems Corp., Suwon, Korea) was used for conducting AFM measurements. Conducting AFM tips (NSC19/Ti−Pt, Mikromasch, Tallinn, Estonia) with a resonance frequency of about 80 kHz and spring constant of about 0.6 N/m were used as the probes. The sample was spun cast on Au film substrate, which is 100 nm in thickness. In this experiment, the typical scan force for topography was about 5.8 nN, and DC voltage is applied from the sample substrate, which was varied between ±1 V, while the tip was grounded. A preamplifier box was used to acquire high signal-to-noise sample current.

Conflict of Interest: The authors declare no competing financial interest.

Acknowledgment. Q. Wang acknowledges funding by CAS "Bairen Ji Hua" Program and "Strategic Priority Research Program" (Grant No. XDA01030200), MOST (Grant No. 2011CB965004), NSFC (Grant No. 21073225, 91023038), Jiangsu Province NSF (BK2012007), and the CAS/SAFEA International Partnership Program for Creative Research Teams. The authors thank Mr. Jie Zhang, Mr. Qi Chen, and Prof. Liwei Chen for *I*−*V* measurements of AgNLs, the authors also thank Prof. Hao Yan and Dr. Shuling Shen for helpful discussion and Mr. Zhong Chen for AFM imaging.

Supporting Information Available: Supporting results mentioned in the text. This material is available free of charge *via* the Internet at http://pubs.acs.org.

REFERENCES AND NOTES

1. Wang, X.; Zhuang, J.; Peng, Q.; Li, Y. A General Strategy for Nanocrystal Synthesis. *Nature* **2005**, *437*, 121124.

2. Burda, C.; Chen, X.; Narayanan, R.; El-Sayed, M. A. Chemistry and Properties of Nanocrystals of Different Shapes. *Chem. Rev.* **2005**, *105*, 1025–1102.
3. Kwon, S. G.; Hyeon, T. Colloidal Chemical Synthesis and Formation Kinetics of Uniformly Sized Nanocrystals of Metals, Oxides, and Chalcogenides. *Acc. Chem. Res.* **2008**, *41*, 1696–1709.
4. Yin, Y.; Alivisatos, A. P. Colloidal Nanocrystal Synthesis and the Organic–Inorganic Interface. *Nature* **2005**, *437*, 664–670.
5. Caruso, F. Nanoengineering of Particle Surfaces. *Adv. Mater.* **2001**, *13*, 11–22.
6. Xia, Y.; Yang, P.; Sun, Y.; Wu, Y.; Mayers, B.; Gates, B.; Yin, Y.; Kim, F.; Yan, H. One-Dimensional Nanostructures: Synthesis, Characterization, and Applications. *Adv. Mater.* **2003**, *15*, 353–389.
7. Talapin, D. V.; Lee, J.-S.; Kovalenko, M. V.; Shevchenko, E. V. Prospects of Colloidal Nanocrystals for Electronic and Optoelectronic Applications. *Chem. Rev.* **2010**, *110*, 389–458.
8. Smith, A. M.; Nie, S. Semiconductor Nanocrystals: Structure, Properties, and Band Gap Engineering. *Acc. Chem. Res.* **2010**, *43*, 190–200.
9. Xia, Y.; Xiong, Y.; Lim, B.; Skrabalak, S. E. Shape-Controlled Synthesis of Metal Nanocrystals: Simple Chemistry Meets Complex Physics. *Angew. Chem., Int. Ed.* **2009**, *48*, 60–103.
10. Park, J.; Joo, J.; Kwon, S. G.; Jang, Y.; Hyeon, T. Synthesis of Monodisperse Spherical Nanocrystals. *Angew. Chem., Int. Ed.* **2007**, *46*, 4630–4660.
11. Frey, N. A.; Peng, S.; Cheng, K.; Sun, S. Magnetic Nanoparticles: Synthesis, Functionalization, and Applications in Bioimaging and Magnetic Energy Storage. *Chem. Soc. Rev.* **2009**, *38*, 2532–2542.
12. Nie, Z.; Petukhova, A.; Kumacheva, E. Properties and Emerging Applications of Self-Assembled Structures Made from Inorganic Nanoparticles. *Nat. Nanotechnol.* **2010**, *5*, 15–25.
13. Li, F.; Josephson, D. P.; Stein, A. Colloidal Assembly: The Road from Particles to Colloidal Molecules and Crystals. *Angew. Chem., Int. Ed.* **2011**, *50*, 360–388.
14. Bai, F.; Wang, D.; Huo, Z.; Chen, W.; Liu, L.; Liang, X.; Chen, C.; Wang, X.; Peng, Q.; Li, Y. A Versatile Bottom-Up Assembly Approach to Colloidal Spheres from Nanocrystals. *Angew. Chem., Int. Ed.* **2007**, *46*, 6650–6653.
15. Kalsin, A. M.; Fialkowski, M.; Paszewski, M.; Smoukov, S. K.; Bishop, K. J. M.; Grzybowski, B. A. Electrostatic Self-Assembly of Binary Nanoparticle Crystals with a Diamond-like Lattice. *Science* **2006**, *312*, 420–424.
16. Lesnyak, V.; Wolf, A.; Dubavik, A.; Borchardt, L.; Voitekhovich, S. V.; Gaponik, N.; Kaskel, S.; Eychmuller, A. 3D Assembly of Semiconductor and Metal Nanocrystals: Hybrid CdTe/Au Structures with Controlled Content. *J. Am. Chem. Soc.* **2011**, *133*, 13413–13420.
17. Qiu, P.; Jensen, C.; Charity, N.; Towner, R.; Mao, C. Oil Phase Evaporation-Induced Self-Assembly of Hydrophobic Nanoparticles into Spherical Clusters with Controlled Surface Chemistry in an Oil-in-Water Dispersion and Comparison of Behaviors of Individual and Clustered Iron Oxide Nanoparticles. *J. Am. Chem. Soc.* **2010**, *132*, 17724–17732.
18. Nykypanchuk, D.; Maye, M. M.; van der Lelie, D.; Gang, O. DNA-Guided Crystallization of Colloidal Nanoparticles. *Nat. Mater.* **2008**, *451*, 549–552.
19. Jones, M. R.; Macfarlane, R. J.; Lee, B.; Zhang, J.; Young, K. L.; Senesi, A. J.; Mirkin, C. A. DNA–Nanoparticle Superlattices Formed from Anisotropic Building Blocks. *Nat. Mater.* **2010**, *9*, 913–917.
20. Henzie, J.; Grünwald, M.; Widmer-Cooper, A.; Geissler, P. L.; Yang, P. Self-Assembly of Uniform Polyhedral Silver Nanocrystals into Densest Packings and Exotic Superlattices. *Nat. Mater.* **2011**, *11*, 131–137.
21. Zhou, Q.; Li, X.; Fan, Q.; Zhang, X.; Zheng, J. Charge Transfer between Metal Nanoparticles Interconnected with a Functionalized Molecule Probed by Surface-Enhanced Raman Spectroscopy. *Angew. Chem., Int. Ed.* **2006**, *45*, 3970–3973.
22. Hu, X.; Wang, T.; Wang, L.; Dong, S. Surface-Enhanced Raman Scattering of 4-Aminothiophenol Self-Assembled Monolayers in Sandwich Structure with Nanoparticle Shape Dependence: Off-Surface Plasmon Resonance Condition. *J. Phys. Chem.* **2007**, *111*, 6962–6969.
23. Yoon, J. H.; Park, J. S.; Yoon, S. Time-Dependent and Symmetry-Selective Charge-Transfer Contribution to SERS in Gold Nanoparticle Aggregates. *Langmuir* **2009**, *25* (21), 12475–12480.
24. Hong, J.-H.; Hwang, Y.-K.; Hong, J.-Y.; Kim, H.-J.; Kim, S.-J.; Won, Y. S.; Huh, S. Facile Preparation of SERS-Active Nanogap-Rich Au Nanoleaves. *Chem. Commun.* **2011**, *47*, 6963–6965.
25. Grouchko, M.; Popov, I.; Uvarov, V.; Magdassi, S.; Kamyshny, A. Coalescence of Silver Nanoparticles at Room Temperature: Unusual Crystal Structure Transformation and Dendrite Formation Induced by Self-Assembly. *Langmuir* **2009**, *25*, 2501–2503.
26. Li, L.; Hu, F.; Xu, D.; Shen, S.; Wang, Q. Metal Ion Redox Potential Plays an Important Role in High-Yield Synthesis of Monodisperse Silver Nanoparticles. *Chem. Commun.* **2012**, *48*, 4728–4730.
27. Yuan, X.; Luo, Z.; Zhang, Q.; Zhang, X.; Zheng, Y.; Lee, J. Y.; Xie, J. Synthesis of Highly Fluorescent Metal (Ag, Au, Pt, and Cu) Nanoclusters by Electrostatically Induced Reversible Phase Transfer. *ACS Nano* **2011**, *5*, 8800–8808.
28. Rao, T. U. B.; Pradeep, T. Luminescent Ag_7 and Ag_8 Clusters by Interfacial Synthesis. *Angew. Chem., Int. Ed.* **2010**, *49*, 3925–3929.
29. Cui, Y.; Wang, Y.; Liu, R.; Sun, Z.; Wei, Y.; Zhao, Y.; Gao, X. Serial Silver Clusters Biomineralized by One Peptide. *ACS Nano* **2011**, *11*, 8684–8689.
30. Liu, G.-K.; Hu, J.; Zheng, P.-C.; Shen, G.-L.; Jiang, J.-H.; Yu, R.-Q.; Cui, Y.; Ren, B. Laser-Induced Formation of Metal–Molecule–Metal Junctions between Au Nanoparticles as Probed by Surface-Enhanced Raman Spectroscopy. *J. Phys. Chem.* **2008**, *112*, 6499–6508.
31. Tang, Z.; Kotov, N. A.; Giersig, M. Spontaneous Organization of Single CdTe Nanoparticles into Luminescent Nanowires. *Science* **2002**, *297*, 237–240.
32. Tang, Z.; Zhang, Z.; Wang, Y.; Glotzer, S. C.; Kotov, N. A. Self-Assembly of CdTe Nanocrystals into Free-Floating Sheets. *Science* **2006**, *314*, 274–278.
33. Hofmeiera, H.; Schubert, U. S. Recent Developments in the Supramolecular Chemistry of Terpyridine–Metal Complexes. *Chem. Soc. Rev.* **2004**, *33*, 373–399.
34. Hoeben, F. J. M.; Jonkheijm, P.; Meijer, E. W.; Schenning, A. P. H. J. About Supramolecular Assemblies of π-Conjugated Systems. *Chem. Rev.* **2005**, *105*, 1491–1546.
35. Miszta, K.; Graaf, J. d.; Bertoni, G.; Dorfs, D.; Brescia, R.; Marras, S.; Ceseracciu, L.; Cingolani, R.; Roij, R. v.; Dijkstra, M.; Manna, L. Hierarchical Self-Assembly of Suspended Branched Colloidal Nanocrystals into Superlattice Structures. *Nat. Mater.* **2011**, *10*, 872–876.
36. Nitzan, A.; Ratner, M. A. Electron Transport in Molecular Wire Junctions. *Science* **2003**, *300*, 1384–1389.
37. Faramarzi, V.; Niess, F. d. r.; Moulin, E.; Maaloum, M.; Dayen, J.-F. o.; Beaufrand, J.-B.; Zanettini, S.; Doudin, B.; Giuseppone, N. Light-Triggered Self-Construction of Supramolecular Organic Nanowires as Metallic Interconnects. *Nat. Chem.* **2012**, *4*, 485–490.
38. Huang, Y.-F.; Zhu, H.-P.; Liu, G.-K.; Wu, D.-Y.; Ren, B.; Tian, Z.-Q. When the Signal Is Not from the Original Molecule To Be Detected: Chemical Transformation of *para*-Aminothiophenol on Ag during the SERS Measurement. *J. Am. Chem. Soc.* **2010**, *132*, 9244–9246.
39. Sun, M.; Xu, H. A Novel Application of Plasmonics: Plasmon-Driven Surface-Catalyzed Reactions. *Small* **2012**, *8*, 2777–2786.
40. Tian, X.; Chen, L.; Xu, H.; Sun, M. Ascertaining Genuine SERS Spectra of *p*-Aminothiophenol. *RSC Adv.* **2012**, *2*, 8289–8292.
41. Zhou, Q.; Zhao, G.; Chao, Y.; Li, Y.; Wu, Y.; Zheng, J. Charge-Transfer Induced Surface-Enhanced Raman Scattering in Silver Nanoparticle Assemblies. *J. Phys. Chem. C* **2007**, *111*, 1951–1954.